


Effect of nanopaper coating on flexural properties of a fire-treated glass fiber reinforced polyester composite

Journal of Composite Materials
0(0) 1–19
© The Author(s) 2016
Reprints and permissions:
sagepub.co.uk/journalsPermissions.nav
DOI: 10.1177/0021998316630584
jcm.sagepub.com


Jamie D Skovron, Jinfeng Zhuge, Jihua Gou and Ali P Gordon

Abstract

Rapid re-launch aerospace vehicles require materials with high specific strength to withstand thermal shock associated with repeated re-entry. Glass fiber reinforced polyester (GRP) composites have rapidly become preferred for high value structural components requiring high specific strength. Their ability to sustain high tensile and impact loads has allowed them to be used as light-transmitting panels and fuselages. Due to service conditions, heat flux strongly alters mechanical properties with exposure time. The effect of including a thermal-barrier coating, in the form of a carbon nanopaper, on the monotonic flexural properties of a GRP composite is analyzed. A series of three-point bend experiments was performed on specimen-sized samples of composites subjected to various levels of heat fluxes across numerous exposure times. Analysis of these experiments reveals trends in the deformation mechanisms of these materials near failure. Correlations of flexural modulus and critical load are used to develop associations to strength.

Keywords

Reinforced composite, exposure energy, rupture, flexure testing

Introduction

The use of composites has grown rapidly due to their attractive mechanical properties in comparison to existing conventional materials. Aircraft manufacturers have incorporated composites into more recent designs as a consequence. Frames of first-generation airplanes were constructed from wood, steel wire, and even silk until it progressed to aluminum. Aluminum alloys have historically been the primary choice due to its good specific strength; however, more recently, the need for higher fuel economy has continued to alter aerospace materials selection.¹ The usage of components fabricated from composites has grown tremendously in current commercial aircrafts. Components of next generation commercial aircrafts have grown from 12 to 50 wt% for composites; while the use of aluminum has decreased from 50 to 20 wt%.² Advanced research has demonstrated through testing that composites have high specific strength at ambient temperatures (below 212°F) and, thus, have grown in popularity. The market pull for light-weight, high-strength design is critical for development activities of re-usable launch vehicles (RLVs). Such spacecrafts must be able to

withstand the cold, near absolute zero, temperature occurring outside of the limits of the stratosphere, but also endure the high temperature of approximately 1260°C (2300°F) during re-entry.³ The spacecraft components should be designed to endure these repetitive thermal exposures for numerous mission cycles while simultaneously or sequentially being mechanically loaded. Re-entry vehicles that have traveled from Earth to Mars have encountered temperatures that exceed 1500°C (2732°F), with the vehicle's nose-cone exhibiting the highest temperature profile.⁴ Without the presence of any form of a thermal-barrier coating, glass fiber reinforced polyester (GRP) composites exhibit pyrolysis between 250°C and 400°C.⁵ It is essential that the selected fuselage materials be able to withstand these thermal shock loads without compromising

Department of Mechanical and Aerospace Engineering, University of Central Florida, USA

Corresponding author:

Ali P Gordon, Department of Mechanical and Aerospace Engineering, University of Central Florida, 4000 Central Florida Blvd., PO Box 162450, Orlando, FL 32816, USA.
Email: apg@ucf.edu

structural integrity. Application of advanced coatings as thermal insulation raises the effective operating temperature of the composite substrate.

The focus of this study is to characterize how thermal barrier carbon nanopaper affects the flexural properties of GRP composites. Nanopaper coatings are applied to a GRP composite, which is then exposed to an applied heat flux, ϕ , at various exposure times, t_{exp} . A heat flux is used to simulate the thermal shock of re-entry temperature loading. Following the return to room temperature (23°C), three-point bend experiments are performed on the coated and uncoated samples. Results of these flexure tests are outputted in the form of force–displacement curves. The mechanical properties related to deformation, strain energy, and rupture behavior of the samples are subsequently derived. Microscopic analysis is conducted to develop damage mechanism maps. Based on the experimental results and microscopy, equations are developed to predict the mechanical response of carbon nanopaper coated GRP composites under service conditions.

A review of the relevant mechanics of materials concepts of GRP composites is detailed in the following section. The candidate material for the current study is discussed next, and the experimental mechanics approach is described later. Subsequent sections provide the data obtained from the three-point bend test and focus on the elastic properties of the GRP composite materials, while later sections cover observations on the rupture trends that were developed and provide an analysis of the residual energy. Lastly density to strength is correlated and a damage mechanism map is detailed. Conclusions are presented in the final section.

Mechanical properties of GRP composites

An increase in the use of fiberglass composites has led to a surge of mechanical characterization of these materials. Models have been developed that predict the mechanical properties of composites while exposed to fire. Research by Gibson et al.⁶ and Mouritz et al.⁷ establishes models that predict the tensile strength failure of fiberglass composites during fire, thereby superimposing thermal and tensile mechanical loading; although these models assume a consistent and uniform fiber composition throughout the experiments. The current study isolates the post-fire mechanical properties through sequential firing then flexure, similar to Bai and Keller.⁸ They modeled the post-fire stiffness of the polyester composites and incorporated the concept of the specimens recuperating some of their mechanical properties during normalized cooling back to room temperature. In addition, this approach allows the designer to approximate the residual properties of the

structure/material. This notion led to the investigation and development of damage mechanism maps illustrated in this work.

A model developed by Gibson et al.⁹ maps the temperature profile of the composite when one side is exposed to a heat source. The authors determined that three processes occur during this type of experiment. The first process is the heat transfer that occurs between the heat source and the composite interface into the body of the material. Once the temperature of the material reaches a critical value, the second process occurs. This process is characterized by a change in the temperature profile due to the decomposition of the matrix which in turn causes heat generation/absorption. The final process is the fluid flow of the volatile gases, caused by the matrix decomposition, towards the heat source/composite interface. The authors mention that agreement between the model and the data is not so accurate when the thickness is below 6 mm; this is due to the critical thickness that is necessary for the progressive degradation process to occur. The authors confirm the notion that the fire retardant effect of composites is a temporary one, existing only until the resin has been gasified. Once the resin has been expunged, the driving force for delaying heat conduction is eradicated.

A post-fire mechanical analysis was also performed by Pering et al.¹⁰ in which the residual tensile strength and stiffness were associated with the percent loss of mass of the specimens. As research techniques advanced in the late 1990s, researchers approached the analysis of the residual strength of post-fire composites by analytically differentiating the material into two layers. One layer would be the unaffected virgin material whose material properties remained unharmed; while the layer exposed to the fire, would be considered the damaged region which possessed little to no residual strength.

The technique of classifying two distinct layers of the composite was explored by Mouritz and Mathys.^{11–16} The authors developed correlations between the thickness of the degraded charred layer, the exposure time, and the time in which charring began. The authors classified the two layers by alternative approaches. The method adopted by Mouritz¹⁴ involved physically measuring the depth of each layer, which in turn led to correlating the thickness to the temperature profile of the specimen.¹⁷ Bai and Keller⁸ improved this procedure by distinguishing a third layer, a transition layer, which could be classified as neither completely damaged nor completely unaffected.

Gardiner et al.¹⁸ carried out a universally accepted method in which the layers are categorized according to the remaining resin content (RRC) criteria. Due to the introduction of heat, a chemical reaction occurs within

the resin matrix that causes a product of toxic gases; which in turn reduces the mass percent and corrupts the structural validity of the composite. With the use of a pulse-echo instrument, the degraded layer is considered any region in which the RRC is less than 80%.¹⁸

Glass-fiber reinforced polyester composites

Materials

GRP composites are composed of multiple layers adhered by an orthophthalic resin. The polyester substrate material used in this study (Figure 1) is reinforced with glass fibers whose specific strength is approximately 0.94 MJ/kg, this value gives the composite its high specific strength.¹⁹ Use of GRP composites in more widespread applications is limited by their poor fire resistivity;²⁰ designers seek a thermal barrier to protect the effectiveness of the material. Carbon nanopaper is selected as the protective barrier that acts not only as a thermal barrier, but absorbs the heat that would otherwise penetrate the composite and compromise the structural integrity.²¹ The current study is focused on whether the carbon nanopaper can considerably protect the flexural strength of the substrate material in the presence of high temperatures. Figure 2 details the dimensions of the uncoated and coated GRP composites.

Carbon nanopaper coatings have become increasingly popular due to their ability to improve the electrical properties of those materials with poor conductivity, such as polymers. Lu et al.²² were able to improve both the electrical properties and thermal conductivity of an epoxy-based resin by coating them with a nanopaper. Chang et al.²³ analyzed the thermal stability and combustion properties of a nanocoating on a plywood substrate. The authors study showed that nanocoatings can effectively decrease the heat rate through the material to protect the underlying and volatile plywood base. As concluded by the studies listed above, the authors of the current study believe that the addition of a nanopaper coating will aid in the protection of the base materials properties.

Vapor grown carbon nanofibers (CNFs) (Pyrograf III PR25-HHT) were supplied by Applied Sciences, Inc. (Cedarville, Ohio), with an average diameter of 80 nm and average surface area of about 50 m²/g. The traditional flame retardant, ammonium polyphosphate (AP423), was supplied by Clariant International Ltd. (Muttens, Switzerland). The Cloisite Na⁺ clay was a pristine form of montmorillonite clay, which was obtained from Southern Clay Products, Inc. (Gonzales, Texas). According to the product specifications, 90 vol.% of dry particles have the size that is less than 13 μm. The exfoliated graphite nanoplatelets (xGnP) were obtained from XG Sciences with a thickness of 5–15 nm. The reinforcement, E-glass fiber mat,

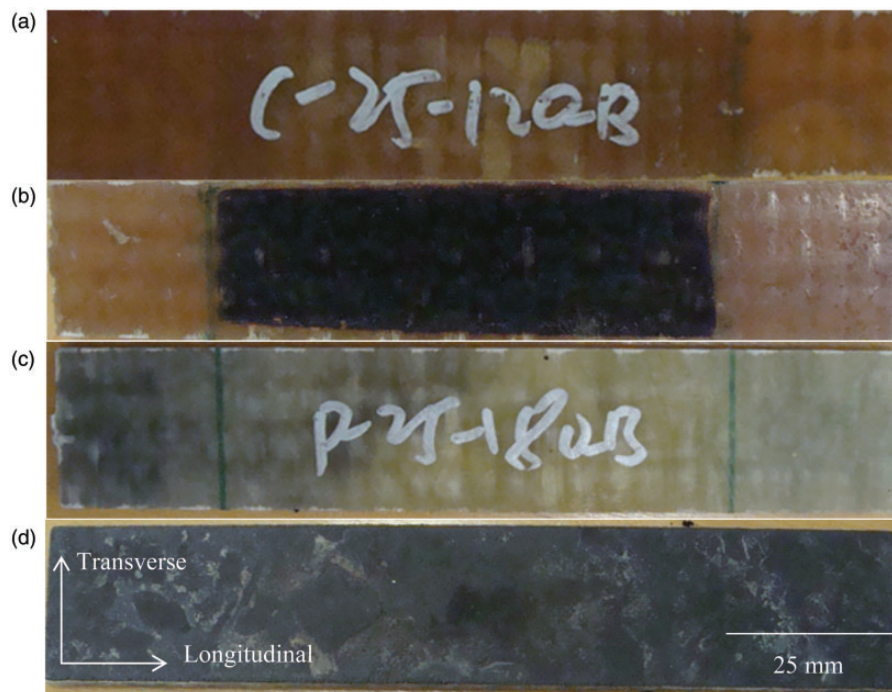


Figure 1. Sample composed of candidate material: (a) uncoated composite (front); (b) uncoated composite (back); (c) coated composite (front); (d) coated composite (back).

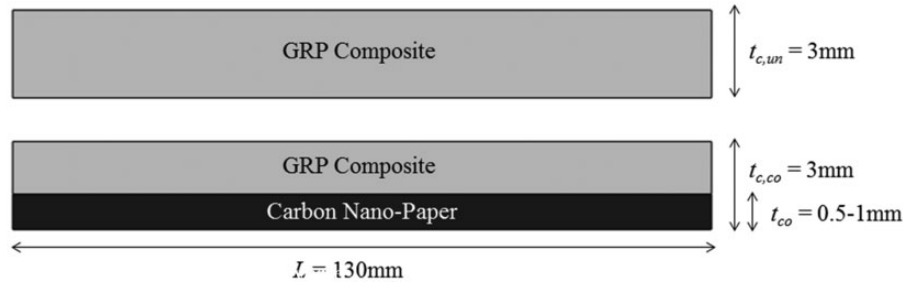


Figure 2. Dimensions of uncoated and coated GRP samples.

Table 1. Composition of hybrid nanopapers and nanocomposites.

Nanocomposites Sample ID	Contents (wt%)			Weight ratios of particles in the nanopaper
	GF	Resin	Nanopaper	
Control	50.6	49.4	0	No paper
1Clay/5CNF/9APP	49.3	47.6	3.1	Clay/CNF/APP = 1/5/9
1xGnP/5CNF/9APP	51.0	45.8	3.2	xGnP/CNF/APP = 1/5/9
3xGnP/5CNF/9APP	51.0	46.0	3.0	xGnP/CNF/APP = 3/5/9

was supplied from Composites One, Inc. (Arlington Heights, Illinois) with a surface density of 800 g/m^2 and an average thickness of 0.85 mm . The matrix material for laminated composites was unsaturated polyester resin. It was a pre-promoted, thixotropic, orthophthalic type of resin that was supplied by PolyGard (Kannur, India) (product code: GP100P; density: 1.1 g/cm^3 ; heat deflection temperature: 75°C). The hardener used in this study was methyl ethyl ketone (MEK) peroxide, and was mixed with resin at a weight ratio of 100:1.

Processing of hybrid nanopaper and nanocomposites

Based on a previous study,²⁴ the as-received CNF, clay, and, xGnP powders were mixed together at the weight ratios shown in Table 1 and dispersed in 1000 mL of distilled water with the aid of surfactant Triton-X100 (3–5 drops). The mixture was then sonicated (Misonix, Model No. S-3000) for 15 min at an amplitude of 60–80 per the controller. After the suspension was well dispersed, the nanopaper was fabricated by filtering the suspension through a vacuum system. It should be noted that due to the lower permeability of the nanopapers containing clay, the fabrication time was much longer than nanopapers containing xGnP. The as-made nanopapers were then dried at 120°C for 2 h. Additionally, the APP powders run the risk of decomposing into smaller particles during sonication, potentially preventing their inclusion in the hybrid nanopaper during filtration. Instead of directly mixing them with CNF, clay, and xGnP in the sonication

process, they were mixed into the polymer matrix using a mechanical shear mixer provided by Cole-Parmer Instrument Company (Vernon Hills, Illinois) (Model No. 50002-30) at 1400 r/min for 4 h, then the mixture was brushed onto the back surface of the dry hybrid paper. Finally, the hybrid nanopaper was coated to the surface of the composite during resin transfer molding (RTM) process. The composition of the hybrid nanopapers and nanocomposites is shown in Table 1.

A Zeiss ULTRA-55 FEG scanning electron microscope (SEM) was utilized to take high magnification images of the material presented in this study. Any reference to the term “transverse” is considered the direction perpendicular to the length, L , of the sample. A reference frame is shown in Figure 1. The SEM pictures shown in Figure 3 are of the unfired, pre-bend test coated sample. At a low magnification it is evident that the candidate material is of a woven-fiber nature, where “CN-P” is the carbon nanopaper, “P-C Inter” is the paper–composite interface, “TF” is the transverse fibers, and “LF” is the longitudinal fibers which run parallel to the length, L . The dark “filler” apparent between each fiber strand is the polyester matrix. The uncoated sample is composed in the same manner, with the exception of the nanopaper.

An equation was formulated to model the geometry of the composite samples. With use of composite dimensions, microscopy, and SEM pictures; the equation was determined to be a sine function to model the centerline of the yarn, and a cosine function to model the widthwise yarn. The geometry is shown in Figure 4

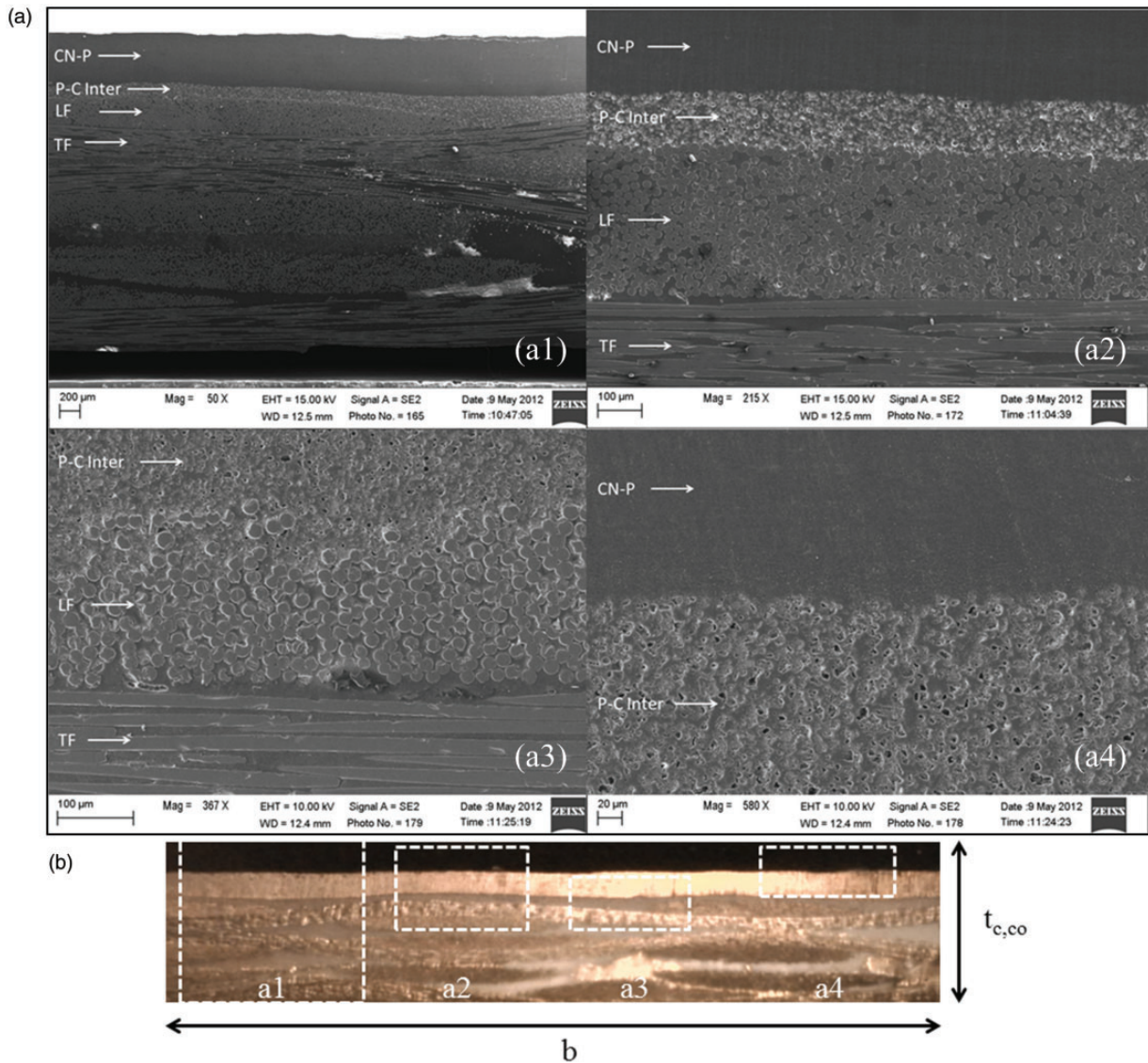


Figure 3. Scanning electron microscope (a) images, (b) location of images on sample of coated GRP material.

and the constants for the equations are displayed in Table 2. Lengthwise and widthwise values are assumed to be the same, because the yarns are assumed to be uniform.

Experimental approach

To determine the post-fire mechanical properties of both the coated and uncoated GRP composites, three-point bend experiments were performed on flat, specimen sized samples. The GRP composites were exposed to predetermined combinations of ϕ and t_{exp} as outlined in Table 3; the firing experimentation was performed using a calorimeter. Some were subjected to firing, while nonfired specimens were implemented to establish a performance baseline. The temperature–time heating

profiles are graphed in Figure 5 for the 25, 35, 50, 75, 100 kW/m² flux levels. Flexure experiments were then performed on samples of the candidate material to determine the effect of firing on the residual mechanical strength. Flexure experiments are preferred on composite samples since the imparted mechanical load bears resemblance to service conditions of the full-scale components of these materials. These flexure tests were administered in accordance with the ASTM D790-10 standard.²⁵ A total of 117 samples, 3 per ϕ - t_{exp} combination, underwent three-point bending (Figure 6) using an electromechanical universal test machine (INSTRON Model No. 3369) with a load capacity of 50 kN. The fire-treated side of the sample was placed face down (i.e. opposite of the middle ram) during the three-point bending test. The support span, L_s , was

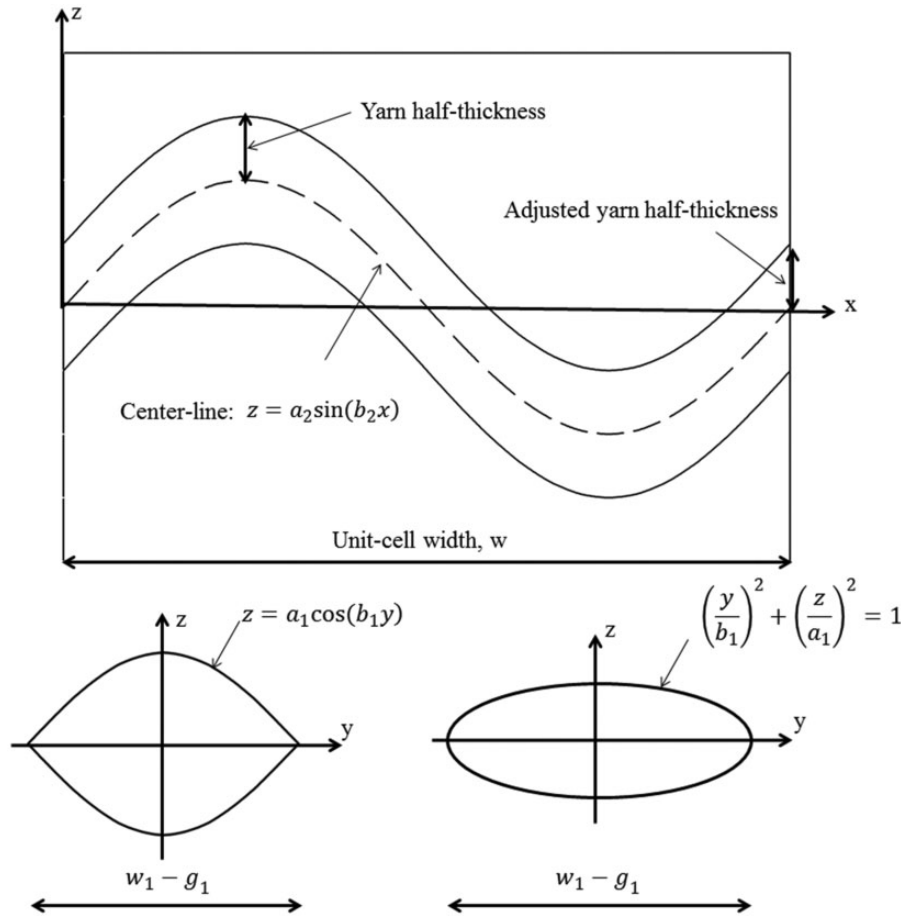


Figure 4. Modeled geometry of lengthwise and widthwise composite yarn.

Table 2. Constants for composite geometry.

Quantity	Lengthwise value	Widthwise value
A1 μm	250	250
A2 μm	250	250
B1 μm^{-1}	0.0010472	0.0010472
B2 μm^{-1}	0.0007306	0.0007306
$w_1 - g_1$ μm	3000	N/A

76 mm and the crosshead motion rate, denoted by $\dot{\delta}$, was 2.4 mm/min. The experiment would cease if either the centerline deflection of the specimen reached 12 mm or there was a dramatic drop in the load–deflection curve.

The mechanical properties that are most relevant to designers relate to elastic response (flexural modulus), strength (ultimate flexural load), and strain energy. Force–deflection data is analyzed to acquire each; for example, the flexural modulus is determined from

$$E_B = \frac{L_S^3 m}{4bt_c^3} \quad (1)$$

Table 3. Heat treatment for the post fire three-point bending test.

Applied heat flux, ϕ (kW/m ²)	Exposure time, t_{exp} (s)
0	0
25	120, 180, 240, 300
35	60, 100, 140, 180
50	40, 80, 120, 150
75	20, 50, 75, 100
100	15, 40, 70, 100

Here, m is the slope of the tangent to the initial straight-line portion of the load–deflection curve (kN/mm), b is the width of the beam tested (mm), and t_c is the thickness of the composite tested (mm). The ultimate flexural load, F_{ult} , is observed as the maximum load on the force–deflection curve. The flexural load at proportional limit, F_{PL} , is shown along with F_{ult} in Figure 7. The strain energy up to the maximum force, denoted by U_{ult} , and the residual strain energy after the maximum

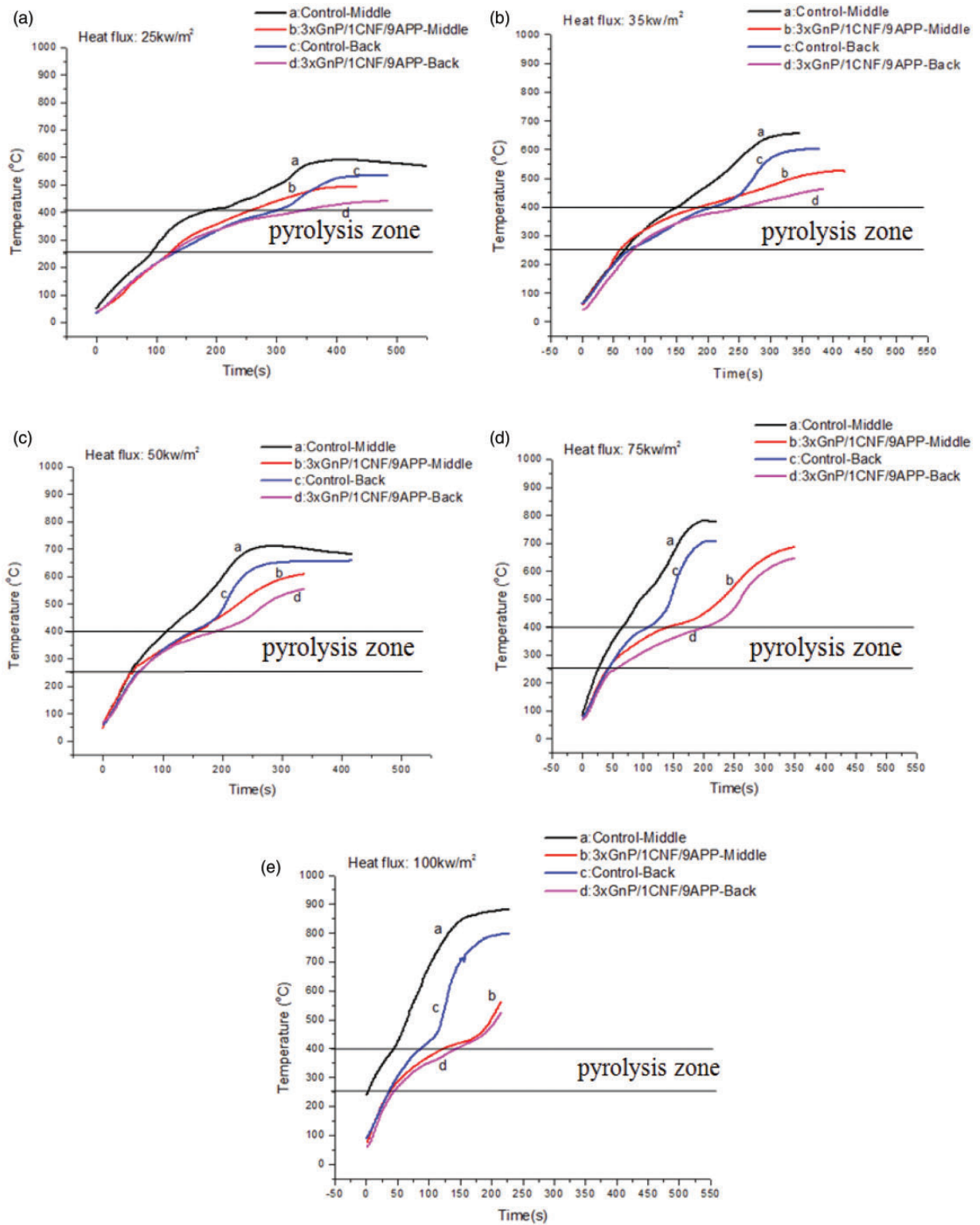


Figure 5. Temperature profiles of the samples subjected to various heat fluxes: (a) 25 kW/m²; (b) 35 kW/m²; (c) 50 kW/m²; (d) 75 kW/m²; (e) 100 kW/m².

force, $U_{residual}$, also shown in the figure, were calculated by implementing the following

$$U = \int_0^{\delta_{ult}} F(\delta) \partial \delta + \int_{\delta_{ult}}^{\delta_{max}} F(\delta) \partial \delta \quad (2)$$

where δ_{ult} is the displacement corresponding to the ultimate force.

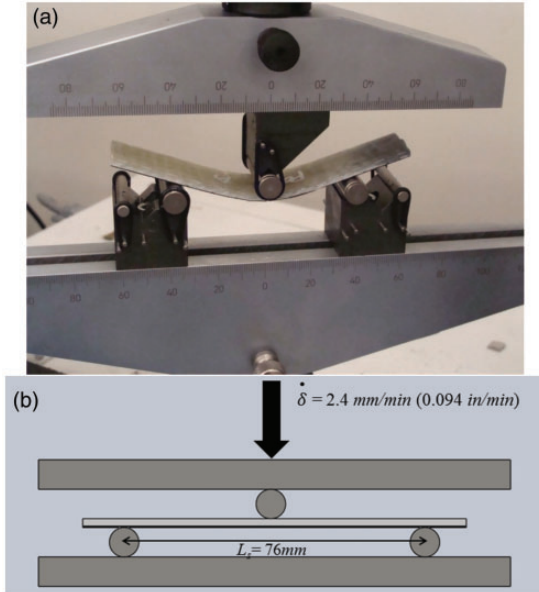


Figure 6. (a) Photograph and (b) schematic of three-point bend experimental setup.

Results

Once the data were obtained from the uniaxial test device in the form of force–displacement curves, post-processing of the data was carried out. Characteristically, experimental analysis on the mechanical properties of composites can pose a challenge due to specimen variability. Despite advancements in the manufacturing of composites, it is common to encounter composites that are anisotropic and heterogeneous. Due to this setback, three experiments were conducted for each ϕ - t_{exp} combination to reduce scatter in the data and provide substantial data.

The force–displacement curves for the control (unfired) samples, along with three ϕ - t_{exp} combinations are shown in Figure 8. It is notable that for most cases, the post-fire uncoated (UC) samples reach a higher force value than the post-fire coated (C) ones, this result is expected since $t_{c,un} > t_{c,co} - t_{co}$. This variation is due to the manufacturing process of RTM in which the volume fraction taken up by the nanopaper coating would otherwise be filled with a high volume of the fibers. Thus, the uncoated samples have a greater amount of matrix and fiber volume, which allows it to bear more loads. The paper coating itself contributes little to no strength to the sample; it merely acts as a thermal barrier.

An observation was noted that independent of the presence of the nanopaper and during a constant flux level, ϕ , an increase in exposure time, t_{exp} , diminishes the mechanical properties of the material. Figure 9

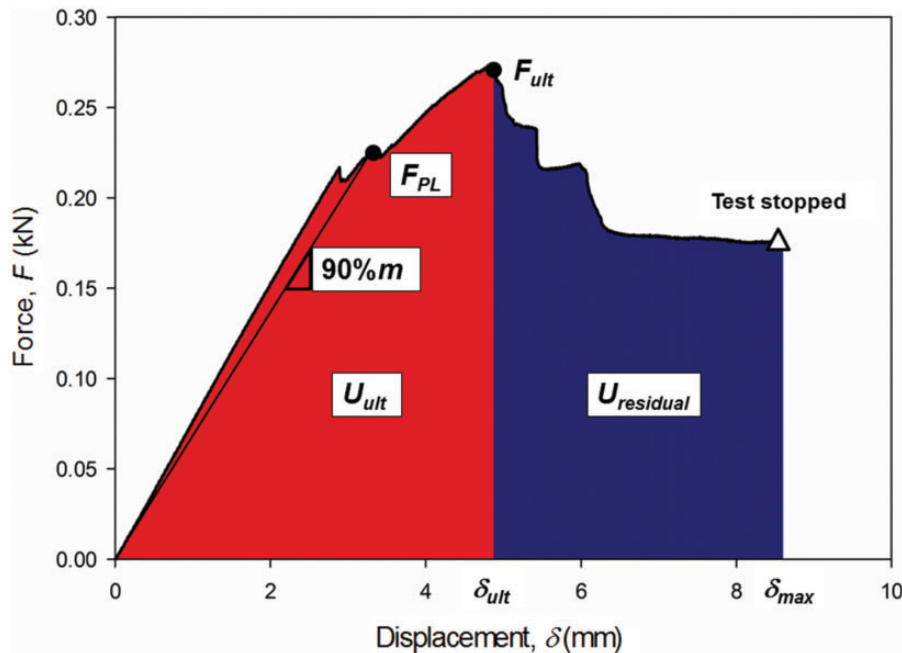


Figure 7. Graphical representation of flexural properties.

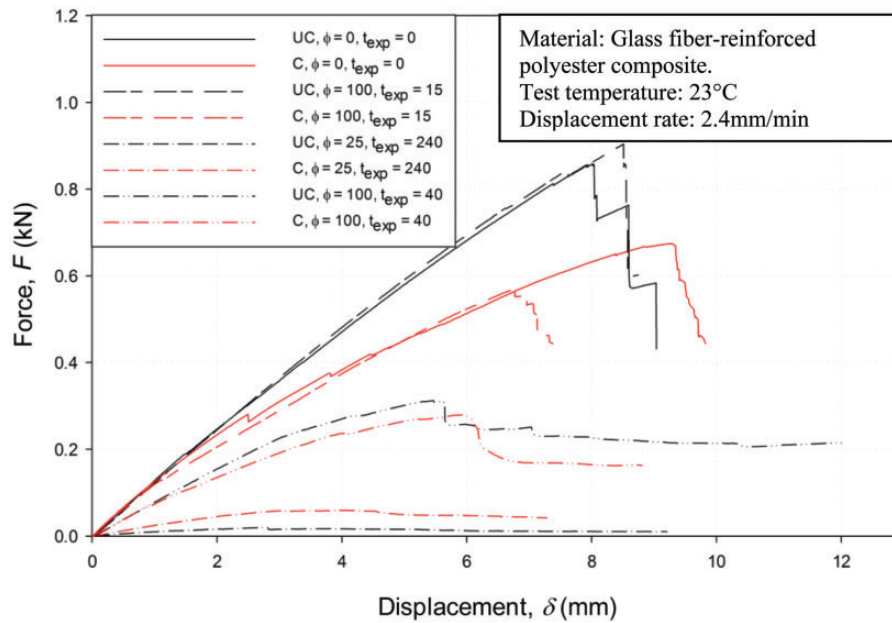


Figure 8. Force–displacement curves for various data sets.

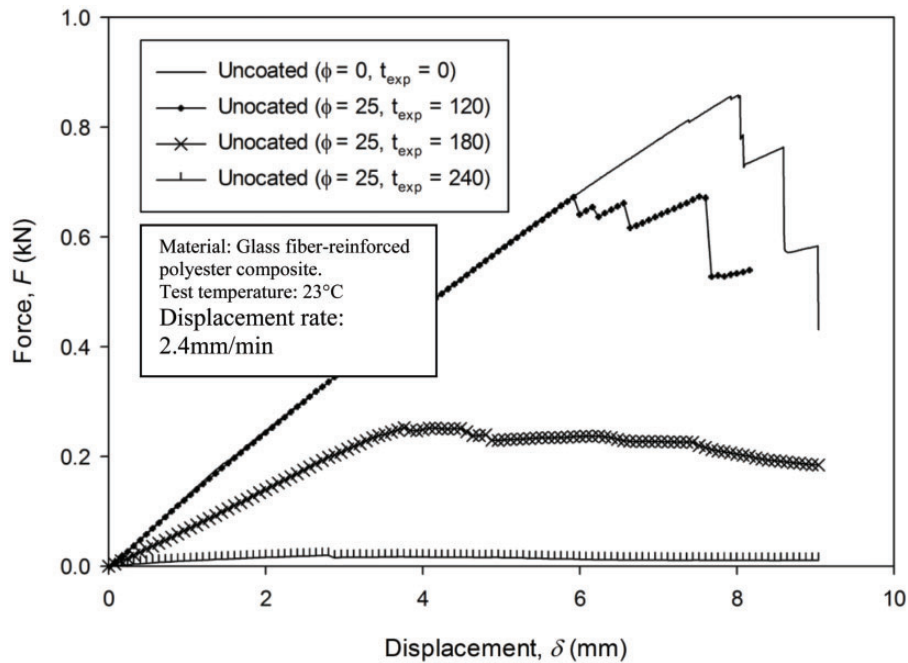


Figure 9. Effect of exposure time, t_{exp} , during constant flux, $\phi = 25 \text{ kW/m}^2$ on uncoated cases.

illustrates this relationship present in the uncoated samples at a constant flux of 25 kW/m^2 and an increase in exposure time. It can be observed that the F_{ult} decreases strongly with increasing t_{exp} , in addition to the balance of U_{ult} and U_{res} also evolving with t_{exp} . This reassures the notion that exposing a sample to a heat source for extended periods of time has a negative effect on the mechanical capabilities of the material.

Elastic modulus

The post-fire elastic modulus, E_B , for each of the samples was calculated to determine the ratio between the force and the deformation of the material. The elastic moduli of the samples were calculated using equation (1). The values for each ϕ - t_{exp} sample set were averaged (unweighted) and used to formulate an equation that

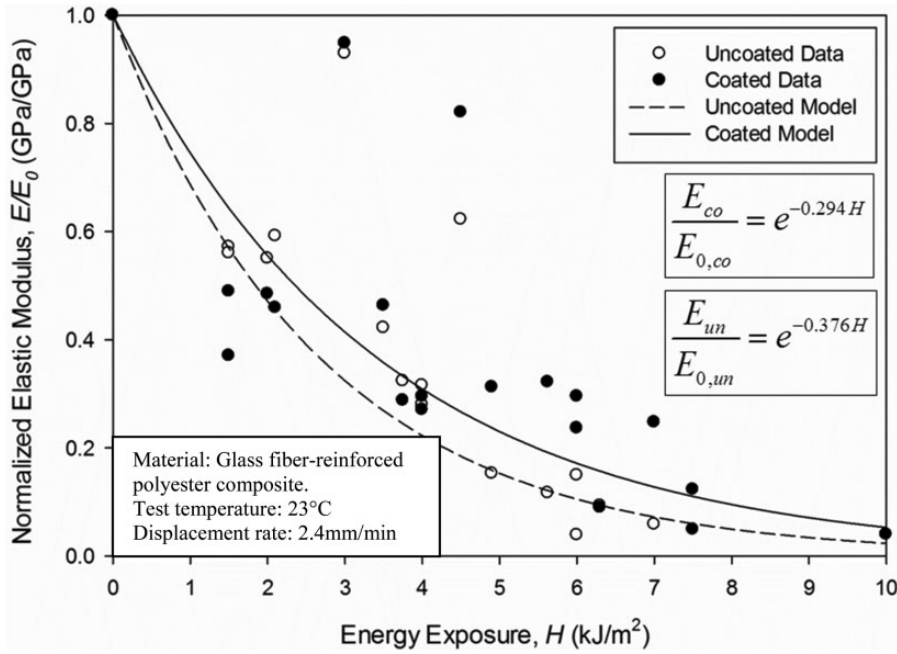


Figure 10. Normalized elastic moduli evolution of fired GRP samples.

predicts the percentage of the un-fired materials elastic modulus, post exposure to heat source, based on the energy exposure, H . The baseline elastic moduli for the control samples are denoted $E_{0,un}$ and $E_{0,co}$, with numerical values of 23.28 GPa and 19.52 GPa, respectively. Post-fire mechanical testing can mask the true mechanical properties of the GRP composites during service. This attribute is present due to the nature of composites as they tend to regain some of their strength after being cooled back down to room temperature.²⁶ For that reason, a temperature–time dependent equation would be less representative of the decomposition of the material; therefore, the equations presented in Figure 10 were developed to depict the evolution of the normalized elastic modulus as a function of the exposure energy, $f(H)$. Energy exposure (kJ/m^2) is defined as follows

$$H = \phi t_{\text{exp}} \quad (3)$$

Past researchers have developed mechanical property models based on separating the composite into two or three layers, but the drawback to these models is the classification of the different layers.^{20,21,24–27} The equations presented in this study correlates the mechanical properties of the uncoated and coated GRP composites based on the energy exposure, shown in Figure 9.

The identical data point pairing from uncoated and coated samples, $\phi = 25 \text{ kW/m}^2$ and $t_{\text{exp}} = 120, 180 \text{ s}$, were excluded due to them posing as outliers in Figure 10. These samples were exposed to the lowest

flux level imposed during this study and thus retain a higher percentage of the control samples elastic moduli due to the low value of energy exposure applied to them. The observed driving factor in all the experiments is the exposure time and not necessarily the flux level. The equations, therefore, are developed with the exclusion of these two data points. The uncoated and coated equations are presented in the same manner with the coated equation having a smaller exponential slope. This smaller slope correlates to retaining a higher percentage of the unfired materials modulus for a given energy exposure. Across the range of energy exposure values, the equations predict that the coated samples have retained nearly 10% greater elastic moduli. The uncoated specimens degrade at a quicker rate, at a given energy exposure of 5 kJ/m^2 for example, the uncoated samples have 30% lower normalized elastic moduli than the coated ones. The uncoated and coated equations possess correlation values of 86.4% and 75.8%, respectively, with the equation forced to predict a normalized value of 1, unchanged, when the energy exposure is zero. The coating is a benefit at low exposure times, but as exposure time approaches infinity, it has little to no effect. A possible solution to decrease the degradation of the elastic modulus at higher exposure times is to increase the thickness of the coating.

Rupture

The effects of the addition of carbon nanopaper on the normalized maximum force and rupture behavior of the

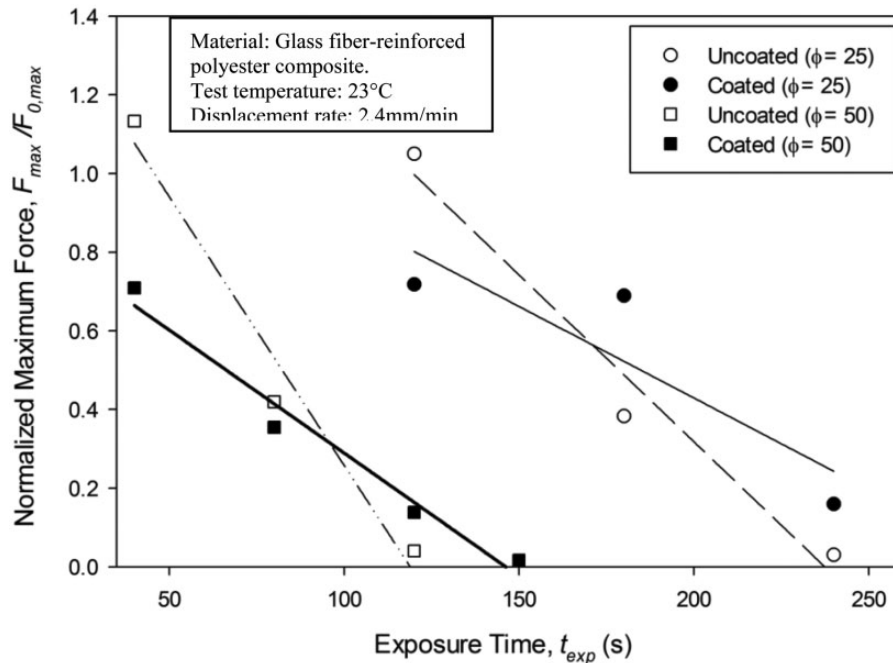


Figure 11. Effects of t_{exp} on the normalized maximum force for fluxes of 25 kW/m^2 and 50 kW/m^2 .

GRP samples are detailed based on the mechanical test data and microscopy. Due to their nature, composites become pliable when exposed to a high temperature, thus the flexural properties measured after the heat flux process may not give accurate properties of how these composites act during fire.²⁸ The characterization behavior of composites is a daunting task due to their anisotropic construction. This structural property alters their heat transfer process as when they burn, they release heat, particle-filled vapors, etc., which is followed by delamination then charring.²⁸ From the force–displacement curve, the maximum force applied during the three-point bend test was tabulated for each specimen sample. Three tests were administered for each combination of ϕ and t_{exp} as shown in Table 3.

The data for each ϕ - t_{exp} combination were averaged and the trends were analyzed. In general it can be concluded that for each flux level set, the longer the exposure time, the lower the maximum force. This is due to the loss of the virgin material properties, and the material becoming “charred” and rendered unusable in service conditions. The maximum forces for the uncoated and coated samples were normalized for each ϕ level. These normalized distributions are shown in Figure 11. One can see from this figure that during a ϕ of 25 kW/m^2 , the maximum force for the paper coated samples exposed to the flux for 180 s have almost three times the original maximum force compared to that of the uncoated samples, normalized values of 0.9598 and 0.3646, respectively. When the samples were exposed to a t_{exp} of 240 s, the normalized values became closer

but the paper samples still maintained a higher percent of their original values, 0.222 compared to 0.029. The same trend can be observed for the samples exposed to a flux level of 50 kW/m^2 . A generalized linear trend, for 25 and 50 kW/m^2 , is displayed to show a negative correlation in the data; it is not stating that the data is linearly associated. Independent of flux level, a steeper negative slope is observed for the uncoated samples; which demonstrates the advantage of the thermal coating.

The physical appearance of the GRP composites after being subjected to a level of heat flux and a three-point bend test is observed in this section. Figure 12(a) shows the composites exposed to a ϕ of 100 kW/m^2 with t_{exp} of 70 s. The uncoated sample has continued to fray, in addition to the expansion of the fibers. This expansion is likely due to the gases escaping during the applied heat flux process.²⁸ The paper on the coated sample has become severely charred and has allowed a greater level of heat flux to penetrate the composite. Fire barrier treatments, such as the carbon nanopaper used in this study, occupy the role of either reflecting the heat back towards the source or delaying the heat penetration towards the underlying composite.²⁸

The extreme end of the flux-time combination is shown in Figure 12(b). The samples shown in Figure 12(b1) and (b2) have been exposed to a level of 100 kW/m^2 for 100 s. Despite both samples having noticeably different physical appearances compared to their associated controls, the coated sample is still in

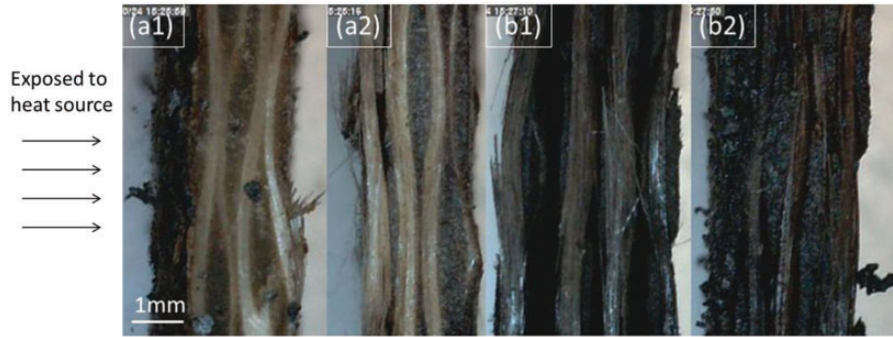


Figure 12. Post-flexural test GRP exposed to 100 kW/m^2 for 70 s (a1) uncoated and (a2) coated samples and 100 kW/m^2 for 100 s for (b1) uncoated and (b2) coated samples.

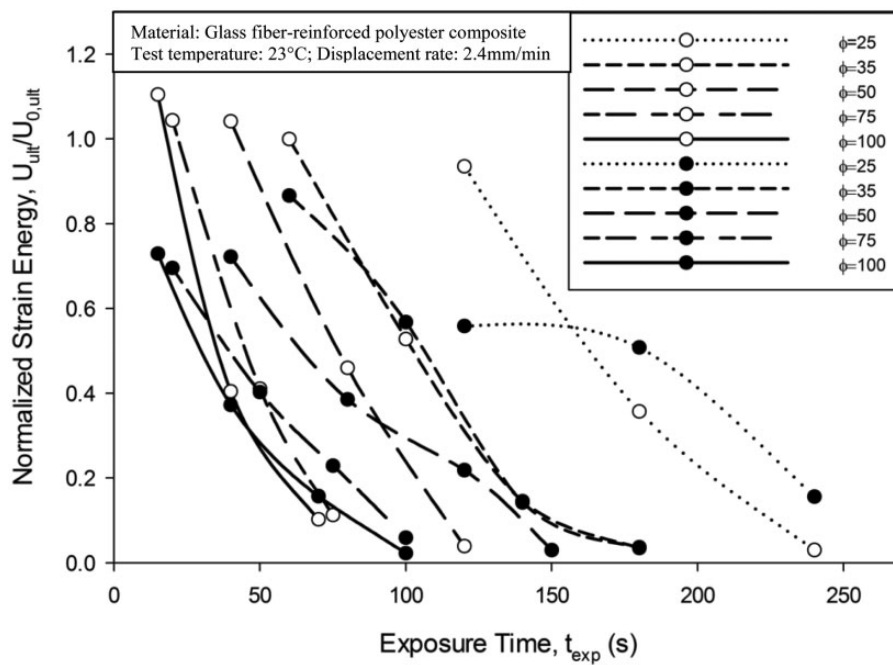


Figure 13. Effects of exposure time on both coated and uncoated material strain energy under flexural loading.

one piece. Figure 12(b1) displays delamination of the composite. Delamination is considered to be the sign of critical failure of a composite; it is characterized by fraying or ply separation due to interlaminar stresses.²⁹ This particular sample is to be considered beyond “failed” due to it experiencing delamination and it being classified as a failed specimen before the three-point bend test. The coated sample was able to endure a three-point bend test, except it only retained a normalized maximum force value of 0.033, equating to 3.3% of the 15 s sample.

Residual energy

Reusable launch vehicles require materials that are able to withstand repeatable loading and unloading during

various temperature levels. The mechanical behavior of the material after it has reached its maximum force, F_{ult} , is investigated to determine the residual energy as well as the unloading conditions that it exhibits for the duration of the experiment. Figure 13 illustrates the exposure time-dependent normalized residual energy absorbed by the specimen according to each flux level for short exposures. It is notable that the slope between the data points for each uncoated or coated flux level. The slope describes the rate at which the residual energy is lost as compared to the control, unfired, sample. Independent of the flux level, it is observed that the residual energies for the coated samples decrease at a slower rate than that of the uncoated samples. The average slope for the uncoated 35, 50, 75, and 100 kW/m^2 fluxes was calculated to be

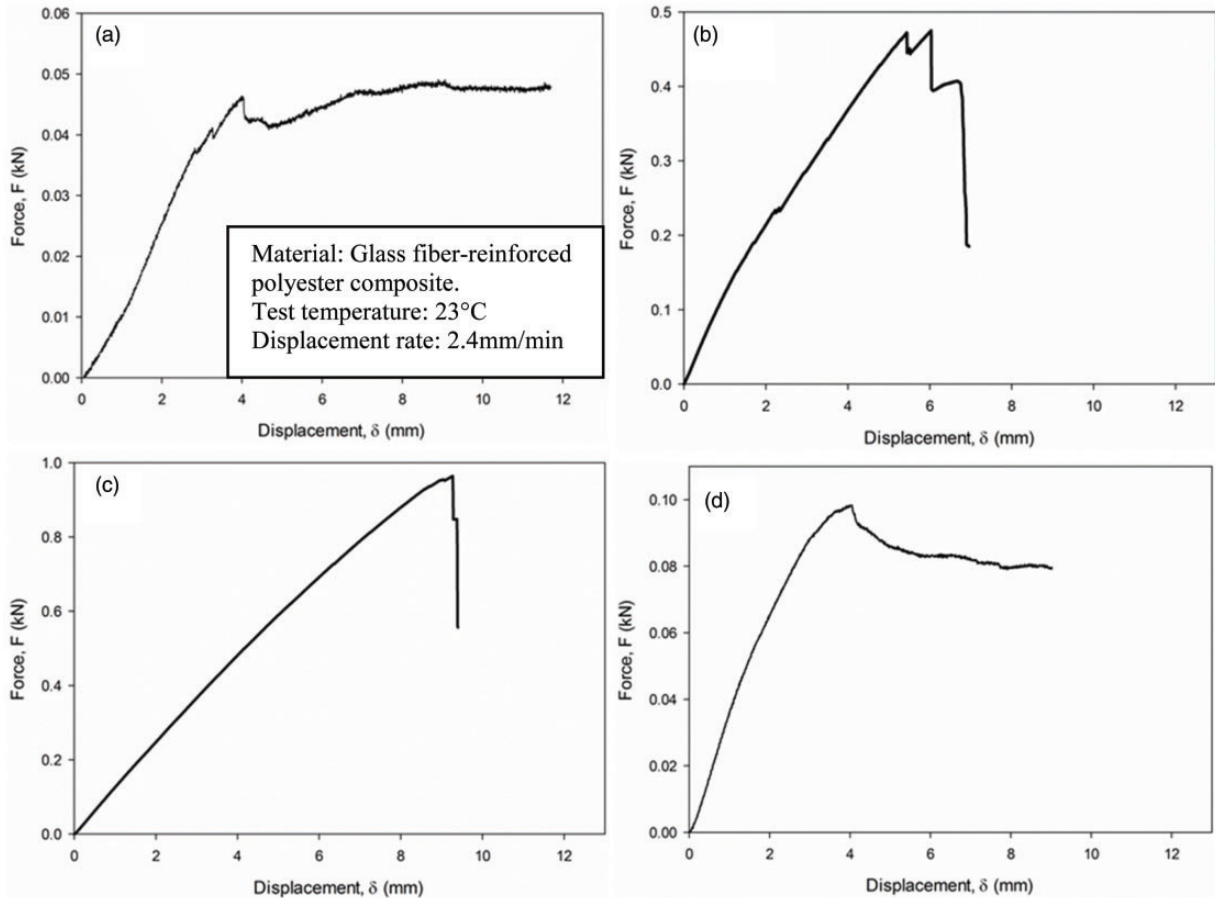


Figure 14. Classifications of unloading conditions: (a) deformed to 12 mm ($UC \phi = 100$, $t_{exp} = 70$); (b) load decreases to 50% of max ($C \phi = 25$, $t_{exp} = 180$); (c) unloaded rapidly ($UC \phi = 50$, $t_{exp} = 40$), and (d) force value converges ($C \phi = 75$, $t_{exp} = 75$).

-0.01887 s^{-1} ; which translates to degrading 1.887% of the residual energy every second. On the other hand, the slope for the coated samples was -0.00999 s^{-1} ; which correlates approximately to a 1% decrease in the residual energy every second. As the uncoated samples lose a higher percentage per second, this confirms the ideology that the presence of the thermal-barrier coating helps retain a higher percentage of the original materials properties. It was noted that once the material had reached its peak force value, it unloaded in one of four ways. These conditions exhibited include, deforming the 12 mm per the ASTM standard; the force value decreasing to 50% of the maximum force; the force unloading too quickly; or the force value converges to a constant value. The most commonly observed unloading trend was the material unloading too quickly due to pop-in occurring to individual glass fibers. Each of the unloading trends is illustrated in Figure 14.

A linear relationship was determined between the normalized maximum force and the normalized residual energy per millimeter. The equations, along with

the data points, are illustrated in Figure 15. These equations are ideal to understand how much residual energy the sample can withstand after it has been subjected to its maximum force. The equations contribute to the focus of this research study, which is aimed at understanding and determining if these materials can withstand re-launches. Based on design criteria of an observed maximum force, the designer can determine how much more residual energy per mm displacement these samples can withstand. The R^2 values for the uncoated and coated equations are 0.99 and 0.96, respectively.

An additional relationship was observed between the normalized stiffness values and the normalized residual energy per millimeter. The equations and data points are shown in Figure 16. Once again, based on the design criteria of in-service stiffness, the designer can determine the residual energy per millimeter displacement remaining. It is interesting to note that the equations intersect at a normalized stiffness value of 0.39. This predicts that at lower normalized stiffness values, the coated samples have a higher value of the

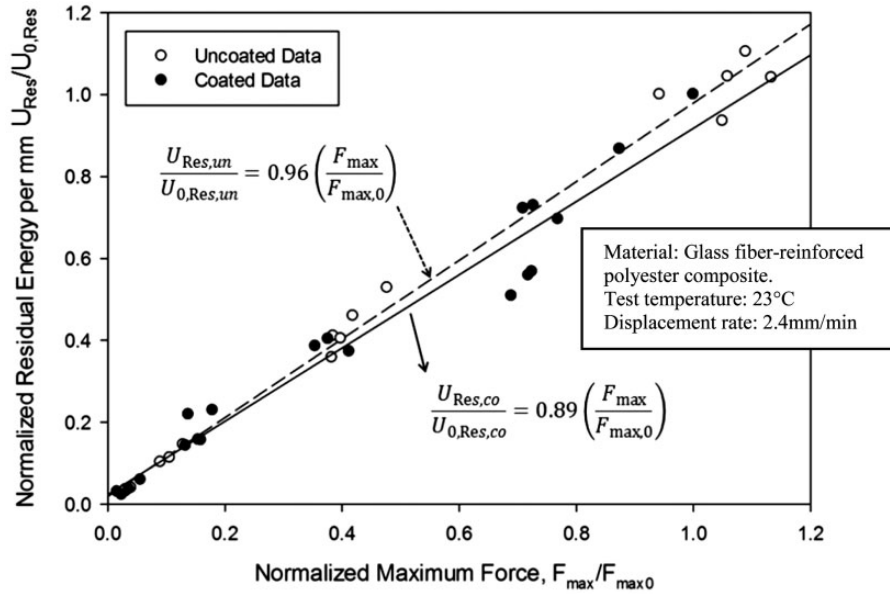


Figure 15. Residual energy per millimeter equations as functions of maximum force.

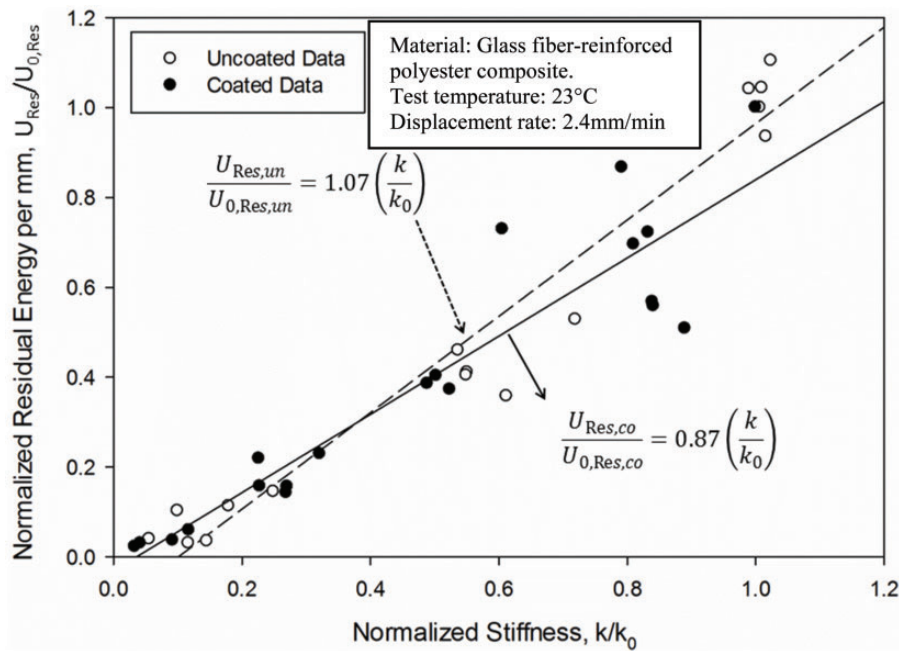


Figure 16. Residual energy per millimeter equations as functions of stiffness.

normalized residual energy per millimeter. The R^2 values for the uncoated and coated equations are 0.96 and 0.87, respectively.

Density-based prediction of post-fire stiffness

The uncoated and coated samples were weighed pre- and post-fire to determine how exposure to a heat source affects the density of the material.

An assumption was made that the volume remained constant throughout the experiments. The samples were weighed as a whole as shown in Figure 1, the gage section was not isolated. The density ratio, equation (4), is defined as the ratio between the post-fire density and the pre-fire density for the corresponding uncoated and coated samples.

$$\text{Density Ratio} = \frac{\rho_{\text{post-fire}}}{\rho_{\text{pre-fire}}} \quad (4)$$

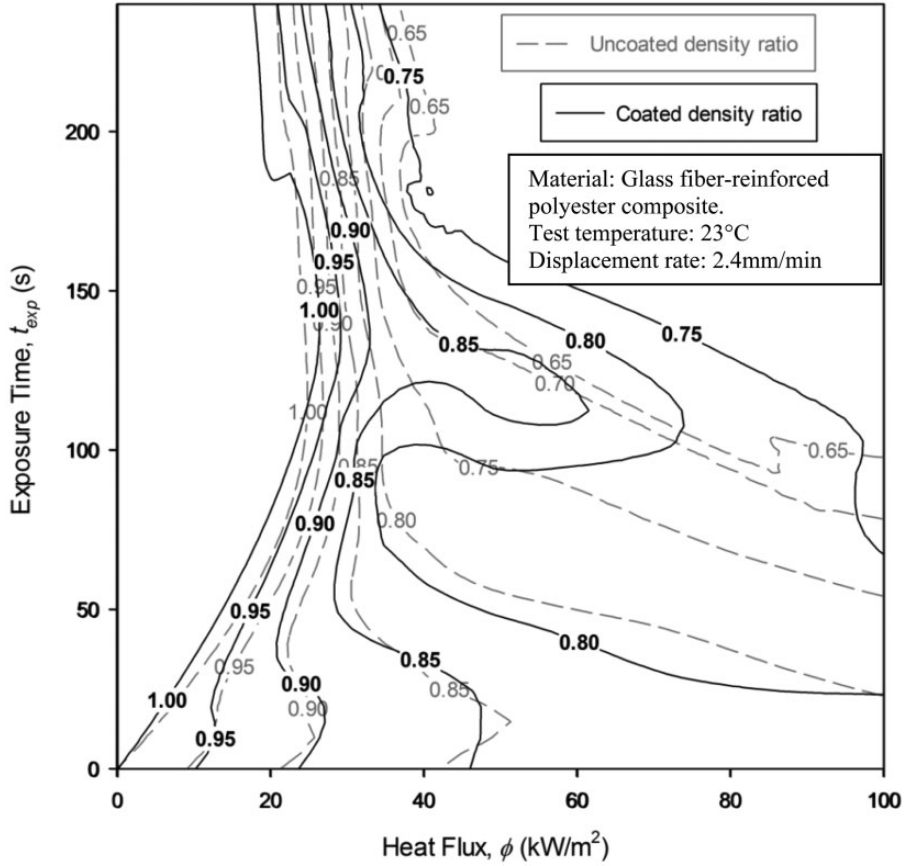


Figure 17. Density ratios as a function of ϕ and t_{exp} .

The pre-fire density value for uncoated samples all had a value of $\rho_{0,un} = 2.02 \times 10^{-3} \text{ g/mm}^3$ and the coated samples had a pre-fire density of $\rho_{0,co} = 2.08 \times 10^{-3} \text{ g/mm}^3$. A contour map displaying the density ratio of the uncoated and coated samples as a function of flux level and exposure time is shown in Figure 17. The data obtained from the contour map was extrapolated to form a plot that maps out the normalized density difference as a function of ϕ and t_{exp} (Figure 18).

Normalized Density Difference

$$= \frac{\left(\frac{\rho_{co,post-fire} - \rho_{un,post-fire}}{\rho_{co,pre-fire} - \rho_{un,pre-fire}} \right)}{\frac{\rho_{un,post-fire}}{\rho_{un,pre-fire}}} \quad (5)$$

The map shows that the biggest density difference, i.e. when the coating is of most benefit, is at a flux range of 25–65 kW/m^2 and a medium to high exposure time of 110–150 s. At higher flux times, the coating is merely charred off instantaneously, and is able to obtain only a slightly higher density percentage than that of the uncoated sample. The peak normalized density difference value was at an exposure time of 110 s at fluxes of

45 and 65 kW/m^2 . At this ϕ - t_{exp} combination, the coating retains 20% more of its corresponding density than that of the uncoated. The lowest differences, i.e. when the coating has little to no effect, are at low exposure times regardless of flux level. The coating's benefit is at a minimum in this section, as it only retains 0.6–3% more of its density compared to the equivalent uncoated samples. The exposure duration is too short to have significant time to significantly damage the sample.

The density ratio is correlated to the normalized stiffness with the unfired ($\phi = 0$, $t_{exp} = 0$) samples used as a baseline. The equations shown in Figure 19 demonstrate that for a given density ratio, the coated samples retained a higher percentage of their original stiffness compared to that of the uncoated. This is an interesting observation due to the uncoated samples possessing a higher volume fraction of composite material, with the coated samples forfeiting structural material for the nanopaper thermal barrier coating. For instance, at a given density ratio of 0.9 the coated equation predicts a normalized stiffness of 0.37, while the uncoated only predicts a value of 0.30. Throughout the entire data range, independent of density ratio, the coated equation always predicts a higher normalized

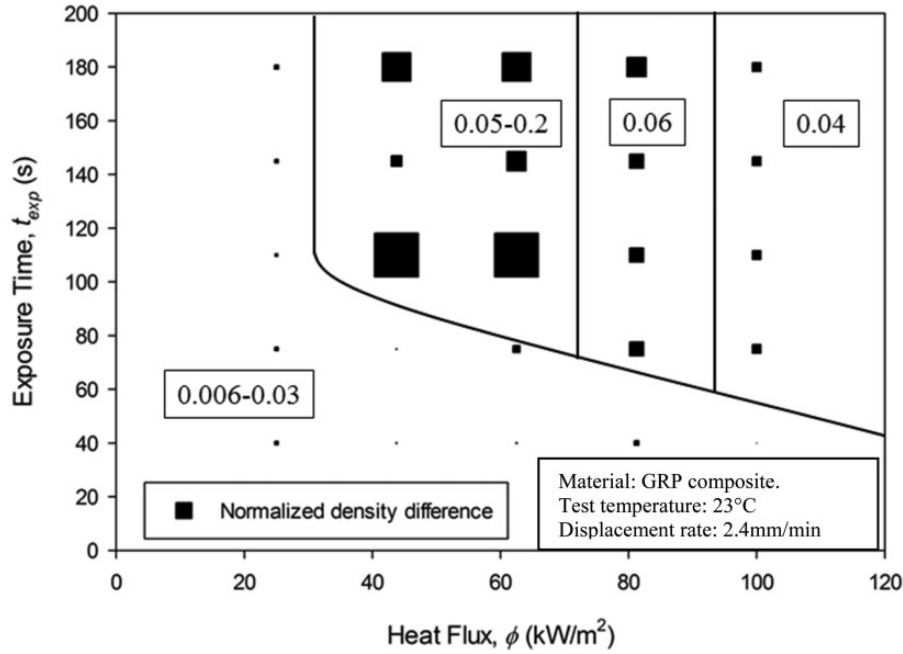


Figure 18. Plot demonstrating benefit of coating based on ϕ - t_{exp} combination.

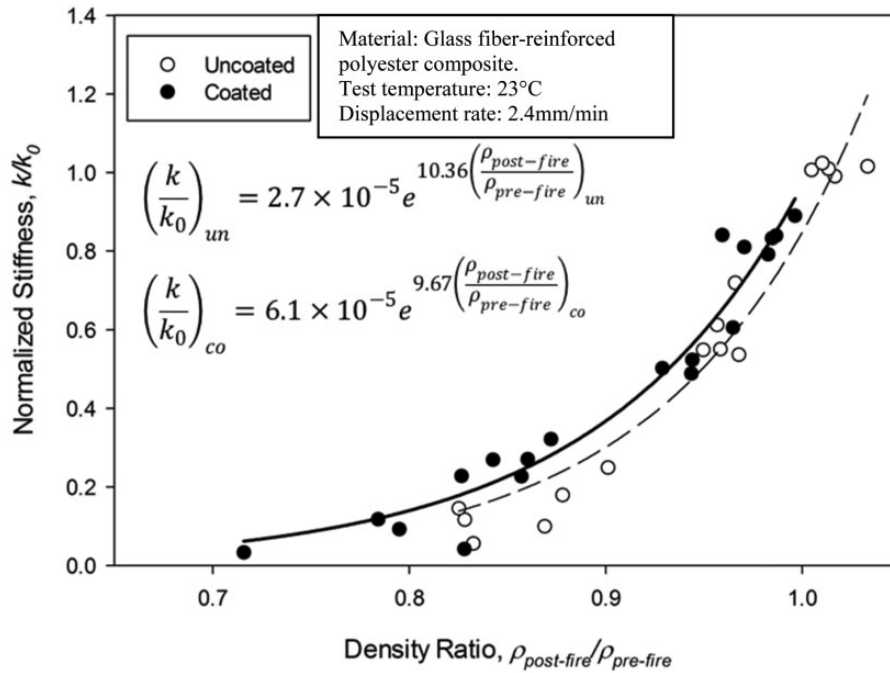


Figure 19. Normalized stiffness values as a function of density ratio.

stiffness. The R^2 values for the uncoated and coated equations are both 0.947.

Damage mechanism maps

Failure in fiber-reinforced composites can occur due to fiber, matrix, or a combined failure of these

constituents. The fibers can fail as an account of tensile, compressive, or shear stresses; while the matrix modes of failure include transverse tensile, transverse compressive, shear, or a combination of these stresses. However, popular methods used to predict the failure method are carried out by analyzing the properties of the composite as a whole, rather than individual fiber

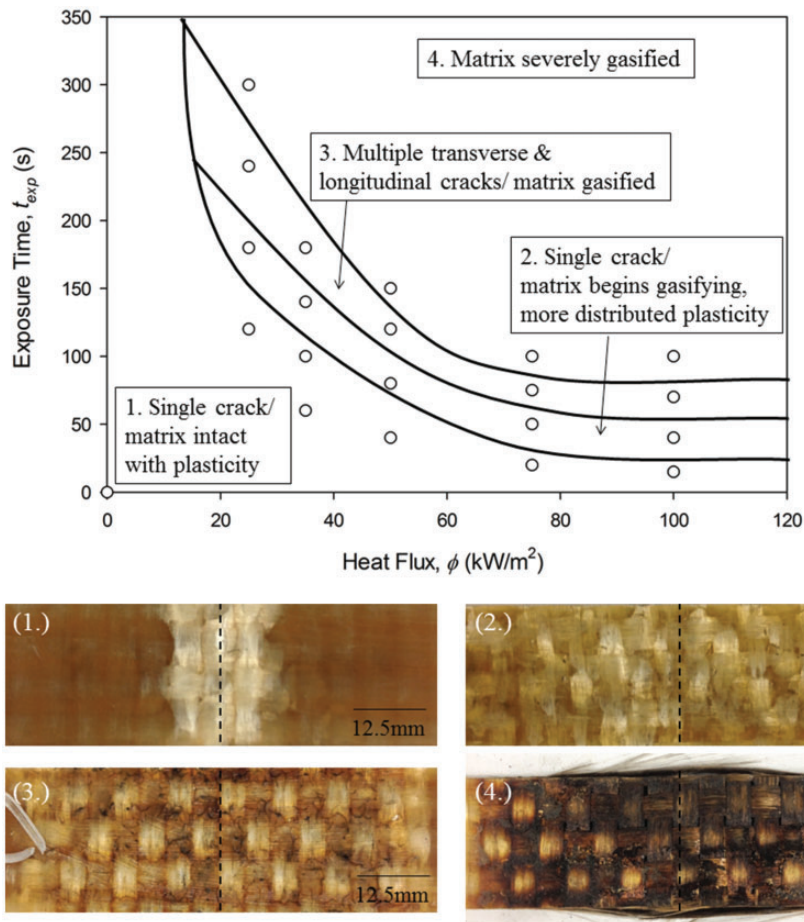


Figure 20. Damage mechanism map of uncoated samples, dotted line represents load application (as shown on load-applied surface).

or matrix components.³⁰ The uncoated and coated samples were plotted according to their corresponding flux and time values, each sample was then visually examined. An uncoated damage mechanism map (Figure 20) was divided into four sections. Samples in the first section failed due to a single crack, the matrix is still intact however it does exhibit minor plasticity. The second section also has a single crack, yet the matrix plasticity has become more distributed with early signs of the matrix gasifying. Samples in the third section possess multiple transverse and longitudinal cracks as the matrix is gasified. The last section is considered failed as the matrix is considered severely gasified.

A similar damage mechanism map was developed for the coated samples (Figure 21). The first section is characterized by a single crack with the nanopaper coating still intact. The second section also exhibits a single crack, yet the coating has begun charring. Gasification is initiated in the third section, along with the coating becoming nonexistent. The fourth and final section, like the uncoated, is considered failed as the coating is nonexistent and the matrix is completely gasified.

Conclusion

GRP composites used for reusable launch vehicles can experience large declines in their mechanical properties after being exposed to a high heat source. The properties decrease as both heat flux and exposure time increase, with the driving variable weighted towards exposure time. The study confirms that the carbon nanopaper helps slow down the degradation process by acting as a thermal barrier between the heat source and the underlying composite. The data suggests that at high exposure times, the paper-coated samples were able to maintain a higher percent of the normalized elastic modulus compared to that of the uncoated samples. Equations to simulate the normalized elastic modulus as a function of energy exposure; and normalized stiffness as a function of density ratio were developed as a guide to understand the properties of GRP composites at various heat flux and exposure time values, with both of these equations outputting a higher value for the coated samples. The damage mechanism maps developed confirm the notion that at high flux, low exposure time situations, the flux is high

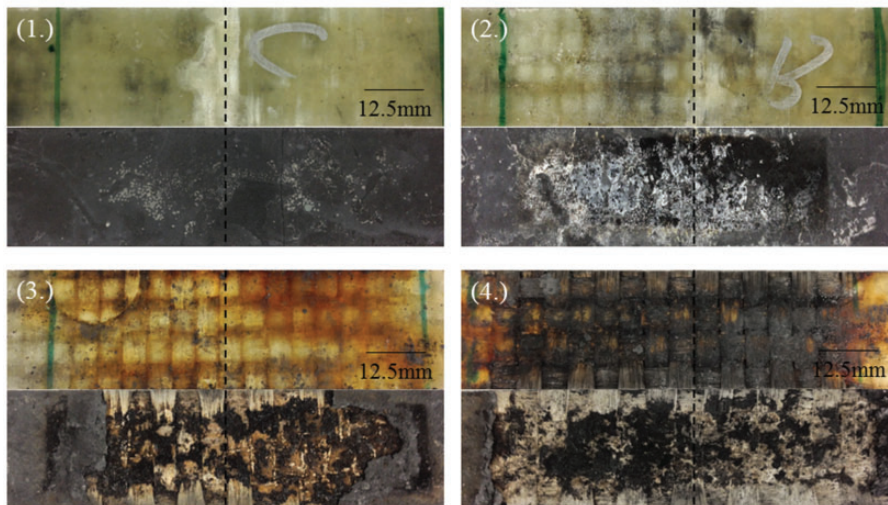
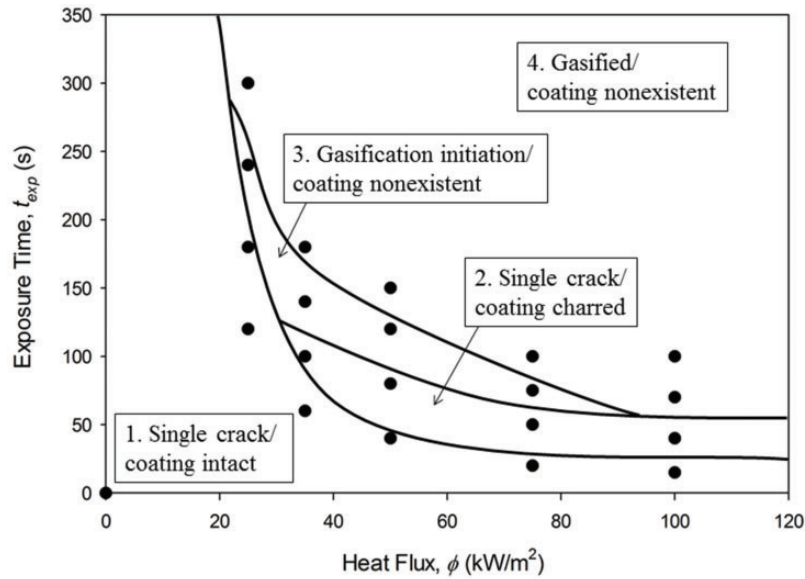


Figure 21. Damage mechanism map of coated samples, dotted line represents load application (top – load applied surface, bottom – heat flux exposure).

enough that it only burns the coating away yet the exposure time is not long enough to affect the underlying laminate. At low flux, high exposure time situations, the exposure time is long enough to give the heat source sufficient time to penetrate the full sample.

Although no cyclic tests have been conducted to compare the effect of the thermal barrier coating, the authors believe that those composites with the thermal barrier coating would have increased fatigue life over those with no coating. This assumption is made due to the increased static performance of those with the added thermal barrier coating and its virgin material strength preservation. Future work will also include, analyzing the coated and uncoated GRP composites under more extreme temperature values, a range from

absolute zero to near 2500°F. One must understand the characterization of these materials at extreme temperatures to ensure proper service.

Declaration of conflicting interests

The author(s) declared no potential conflicts of interest with respect to the research, authorship, and/or publication of this article.

Funding

The materials presented here are based upon work supported by Office of Naval Research under grant number N00014-09-1-0429 and Federal Aviation Administration Center of Excellence for Commercial Space Transportation (FAA COE-CST-AST) under grant number 10CCSTUCF002.

References

1. Ashby MF. *Materials selection in mechanical design*, 4th ed. Burlington, MA: Butterworth-Heinemann, 2011.
2. Hale J. Boeing 787 from the ground up. *Aero Magaz* 2006; 4: 17–24.
3. Kullman E. Investigation of high temperature antenna designs for space shuttle. In: *Antennas and propagation society international symposium*, Vol. 12, 1974, pp. 210–213.
4. Rawal S. Metal-matrix composites for space applications. *J Miner Metals Mater Soc* 2001; 53: 14–17.
5. Ferreira JM, Errajhi OAZ and Richardson MOW. Thermogravimetric analysis of aluminized E-glass fiber reinforced unsaturated polyester composites. *Polym Test* 2006; 25: 1091–1094.
6. Gibson AG, Wu YS, Evans JT, et al. Laminate theory analysis of composites using load in fire. *J Compos Mater* 2006; 40: 639–658.
7. Mouritz AP, Feih S, Mathys Z, et al. Mechanical property degradation of naval composite materials in fire. In: Couchman L and Mouritz AP (eds) *Modeling of naval composite structures in fire*. Melbourne: Acclaim Printing, 2006, pp.51–108.
8. Bai Y and Keller T. Modeling of post-fire stiffness of E-glass fiber-reinforced polyester composites. *Compos Part A: Appl Sci Manuf* 2007; 38: 2142–2153.
9. Gibson AG, Wu Y-S, Chandler HW, et al. A model for the thermal performance of thick composite laminates in hydrocarbon fires. *Revue de L'Institut Francais du Petrole* 1995; 50: 69–74.
10. Pering GA, Farrell PV and Springer GS. Degradation of tensile and shear properties of composites exposed to fire or high temperatures. *J Compos Mater* 1980; 14: 54–68.
11. Gibson AG, Wright PNH, Wu YZ, et al. Modeling residual mechanical properties of polymer composites after fire. *Plast Rub Compos: Macromol Eng* 2003; 32: 81–90.
12. Mouritz AP and Mathys Z. Post-fire mechanical properties of marine polymer composites. *Compos Struct* 1999; 47: 643–653.
13. Mouritz AP. Post-fire properties of fiber-reinforced polyester, epoxy and phenolic composites. *J Mater Sci* 2002; 37: 1377–1386.
14. Mouritz AP. Mechanical properties of fire damaged glass-reinforced phenolic composites. *Fire Mater* 2000; 24: 67–75.
15. Mouritz AP. Simple models for determining the mechanical properties of burnt FRP composites. *Mater Sci Eng* 2003; A359: 237–246.
16. Mouritz AP and Mathys Z. Post-fire mechanical properties of glass-reinforced polyester composites. *Compos Sci Technol* 2001; 61: 475–490.
17. Keller T, Tracy C and Zhou A. Structural response of liquid-cooled GFRP slabs subjected to fire. Part I: Material and post-fire modeling. *Compos Part A: Appl Sci Manuf* 2006; 37: 1286–1295.
18. Gardiner CP, Mathys Z and Mouritz AP. Post-fire structural properties of burnt GRP plates. *Marine Struct* 2004; 17: 53–73.
19. Wambua P, Ivens J and Verpoest I. Natural fibres: Can they replace glass in fibre reinforced plastics? *Compos Sci Technol* 2003; 63: 1259–1264.
20. Mouritz AP and Mathys Z. Post-fire mechanical properties of glass-reinforced polyester composites. *Compos Sci Technol* 2001; 6: 475–490.
21. Zhuge J. Fire retardant evaluation of carbon nanofiber/graphite nanoplatelets nanopaper-based coating under different heat fluxes. *Compos Part B: Eng* 2012; 43: 3293–3305.
22. Lu H, Huang WM and Leng J. Functionally graded and self-assembled carbon nanofiber and boron nitride in nanopaper for electrical actuation of shape memory nanocomposites. *Compos Part B: Eng* 2014; 62: 1–4.
23. Chang H, Kuo ZH, Tsai KC, et al. Analysis on properties of water-based fire-retardant nano-coatings. *Adv Mater Res* 2011; 311–313: 1985–1992.
24. Tang Y, Zhuge J, Lawrence J, et al. Flame retardancy of carbon nanofiber/intumescent hybrid paper based fiber reinforced polymer composites. *Polym Degrad Stab* 2011; 5: 760–770.
25. ASTM Standard D790. *Standard test methods for flexural properties of unreinforced and reinforced plastics and electrical insulating materials*. West Conshohocken, PA: ASTM International, 2010.
26. Kandare E, Kandola BK, Myler P, et al. Thermo-mechanical responses of fibre-reinforced epoxy composites exposed to high temperature environment: I. *J Compos Struct* 2010; 26: 3093–3114.
27. Bai Y, Keller T and Vallee T. Modeling of stiffness of FRP composites under elevated and high temperatures. *Compos Sci Technol* 2008; 68: 3099–3106.
28. Sorathia U, Beck C and Dapp T. Residual strength of composites during and after fire exposure. *J Fire Sci* 1993; 11: 255–270.
29. Mallick PK. *Fiber-reinforced composites: Materials, manufacturing, and design*, 3rd ed. Boca Raton, FL: CRC Press, 2008, p.474.
30. Soden PD, Hinton MJ and Kaddour AS. A comparison of the predictive capabilities of current failure theories for composite laminates. *Compos Sci Technol* 1998; 58: 1225–1254.